GEOPHYSICS, VOL. 86, NO. 2 (MARCH-APRIL 2021); P. F9–F23, 13 FIGS., 3 TABLES.
10.1190/GEO2020-0196.1

Implementation of the Marchenko multiple elimination algorithm

Jan Thorbecke[1], Lele Zhang[1], Kees Wapenaar[1], and Evert Slob[1]

ABSTRACT

The Marchenko multiple elimination (MME) and transmission compensation schemes retrieve primary reflections in the two-way traveltime domain without model information or using adaptive subtraction. Both schemes are derived from projected Marchenko equations and are similar to each other, but they use different time-domain truncation operators. The MME scheme retrieves a new data set without internal multiple reflections. The transmission-compensated Marchenko multiple elimination scheme does the same and additionally compensates for transmission losses in the primary reflections. Both schemes can be solved with an iterative algorithm based on a Neumann series. At each iteration, a convolution or correlation between the projected focusing function and the measured reflection response is performed, and, after each convolution or correlation, a truncation in the time domain is applied. After convergence, the resulting projected focusing function is used for retrieving the transmission-compensated primary reflections and the projected Green's function is used for the physical primary reflections. We have determined that internal multiples are removed by using time-windowed input data that only contain primary reflections. We evaluate both schemes in detail and develop an iterative implementation that reproduces the presented numerical examples. The software is part of our open-source suite of programs and fits into the Seismic Unix software suite of the Colorado School of Mines.

INTRODUCTION

The Marchenko algorithm can eliminate internal multiple reflections in reflection data (Behura et al., 2014; Slob et al., 2014; Wapenaar et al., 2014a). For these schemes, up- and downgoing focusing functions, with a focal point in the subsurface, are retrieved by solving the coupled Marchenko equations. Green's functions can be computed once these focusing functions are known. A virtual reflection response, with an acquisition surface placed in the subsurface, can be obtained by deconvolving the solved up- and downgoing Green's functions (Broggini et al., 2014; Slob et al., 2014; Wapenaar et al., 2014b; Van der Neut et al., 2015b; Matias et al., 2018). Based on the constructed virtual reflection response, an artifact-free image at the focal point can be created. The measured single-sided reflection response and a smooth velocity model are required for the implementation of these Marchenko redatuming schemes. The iterative implementation of the Marchenko redatuming scheme has been discussed in detail, and the software has been published by Thorbecke et al. (2017). Lomas and Curtis (2019) illustrate the concepts of the Marchenko method for redatuming and imaging with reproducible scripts in MATLAB. A Marchenko implementation is also part of PyLops (Ravasi and Vasconcelos, 2020).

A wide range of applications has been developed that are based on solutions of the Marchenko equations. Singh et al. (2015) modify the Marchenko scheme to account for free-surface-related multiple reflections. Dukalski and de Vos (2017), Ravasi (2017), and Singh et al. (2017) extend the Marchenko redatuming scheme for marine seismic data and show its performance in numerical and field examples. Meles et al. (2018) propose a different time-focusing condition of the Marchenko redatuming scheme for retrieval of virtual plane-wave responses. The plane-wave scheme allows multiple-free imaging at a fraction of the computational cost of the regular Marchenko scheme. Wapenaar et al. (2017) derive the homogeneous Green's function retrieval scheme from the Marchenko equations, in which the homogeneous Green's function between any two points inside a medium can be retrieved from the measured single-sided reflection response. Ravasi et al. (2016), Jia et al. (2018), Staring et al. (2018), Mildner et al. (2019), and Pereira et al. (2019) apply the Marchenko method successfully on field data. Sripanich et al. (2019) derive a method that can es-

Peer-reviewed code related to this article can be found at http://software.seg.org/2021/0002.
Manuscript received by the Editor 1 April 2020; revised manuscript received 20 August 2020; published ahead of production 24 November 2020; published online 19 February 2021.
[1]Delft University of Technology, Department of Geoscience and Engineering, P.O. Box 5048, Delft 2600 GA, The Netherlands. E-mail: J.W.Thorbecke@tudelft.nl (corresponding author); L.Zhang-1@tudelft.nl; c.p.a.wapenaar@tudelft.nl; e.c.slob@tudelft.nl.

timate the initial focusing functions from data that does not rely on a velocity model for mildly varying media. Mildner et al. (2019) develop a method to estimate a source wavelet from the Marchenko focusing functions that enables more precise Marchenko redatuming. The Marchenko redatuming scheme also has been extended from acoustic media to elastic (da Costa Filho et al., 2014; Wapenaar, 2014) and dissipative (Slob, 2016) media. Lomas et al. (2020) develop a vertical seismic profile (VSP) Marchenko imaging methodology that enables imaging of horizontal and vertical structures.

Marchenko-based methods also have been developed for dealing with internal multiple reflections in the two-way traveltime domain. Meles et al. (2015) combine convolutional interferometry with the Marchenko redatuming scheme to approximately attenuate internal multiple reflections. Meles et al. (2017) and da Costa Filho et al. (2017) introduce a method that can directly construct primaries without the need for adaptive subtraction. Van der Neut and Wapenaar (2016) project the coupled Marchenko equations to the surface by convolving both sides of the equations with the initial Green's function to reduce the requirement of model information. The schemes for Marchenko multiple elimination (MME) (Zhang and Staring, 2018) and transmission-compensated Marchenko multiple elimination (T-MME) (Zhang et al., 2019) are derived from the projected equations to eliminate all orders of internal multiple reflections without model information or adaptive subtraction. In this case, the projected focusing functions are regarded as regular filters that are defined within an offset independent time window; hence, they are truly model independent. The MME scheme retrieves the primaries from the reflection data, whereas T-MME retrieves the transmission-compensated primaries from the upgoing filter function. The MME scheme also has been tested on numerical and field data (Zhang and Slob, 2020a). The examples in Zhang and Slob (2019) show that all orders of internal multiple reflections are successfully eliminated by both schemes. Zhang and Slob (2019) extend the MME scheme to account for free-surface-related multiple reflections. Thus, free-surface and internal multiple reflections are removed in one step without adaptive subtraction or model information.

In this paper, we describe the implementation of the MME and T-MME schemes in detail. Both schemes eliminate internal multiple reflections without the need for model information or adaptive subtraction. Only a reflection response without a source wavelet and free-surface-related multiple reflections is required as input. This paper is organized as follows. In the "Theory" section, we briefly review the equations of the MME and T-MME schemes. In the implementation section, the processing details are explained step by step, and this section provides a user's first step with the MME and T-MME schemes. The mechanism of the algorithm is illustrated with a simple three-reflector 1.5D horizontally layered model. This simple model is chosen to keep the number of events limited and to allow for an explanation that can be followed more easily. The method is not limited to simple models and can be applied successfully to complicated 3D media as well (Zhang and Slob, 2020c).

The software accompanying this paper contains scripts and source code to reproduce all of the numerical examples presented in this paper. The code also can be found at its GitHub repository (Thorbecke et al., 2017; Thorbecke and Brackenhoff, 2020), where the most recent version and latest developments are available. The commands to reproduce all figures in this paper can be found in the directory marchenko/demo/mme. The README_PRIMARIES in that directory explains in detail how to run the scripts. A more complicated (lateral varying) model can be found in the directory marchenko/demo/twoD. This example will take several hours to compute the reflection data and is not discussed here. To reproduce the figures and to carry out a few pre- and postprocessing steps, Seismic Unix (Cohen and Stockwell, 2016) is required.

THEORY

In this section, we give a brief overview of the theory of the MME and T-MME schemes. The acquisition surface is located at the surface boundary $\partial\mathbb{D}_0$. The reflection response $R(\mathbf{x}_0, \mathbf{x}_0', t)$ is measured with the source and receiver positioned at $\mathbf{x}_0'$ and $\mathbf{x}_0$, which is free from free-surface-related multiple reflections and source wavelet. The time is denoted t.

MME

As presented by Zhang et al. (2019), we give the equations of the MME scheme as

$$R_t(\mathbf{x}_0', \mathbf{x}_0'', t = t_2) = R(\mathbf{x}_0', \mathbf{x}_0'', t = t_2) + \sum_{m=1}^{\infty} M_{2m}(\mathbf{x}_0', \mathbf{x}_0'', t = t_2, t_2), \quad (1)$$

with

$$\begin{aligned} M_{2m}(\mathbf{x}_0', \mathbf{x}_0'', t, t_2) = &\int_{t'=0}^{+\infty} \int_{\partial\mathbb{D}_0} R(\mathbf{x}_0''', \mathbf{x}_0', t') H(t - t' - \varepsilon) \mathrm{d}\mathbf{x}_0''' \mathrm{d}t' \\ &\times \int_{t''=0}^{+\infty} \int_{\partial\mathbb{D}_0} R(\mathbf{x}_0, \mathbf{x}_0''', t'') H(t' - t + t_2 - t'' - \varepsilon) \\ &\times M_{2(m-1)}(\mathbf{x}_0, \mathbf{x}_0'', t - t' + t'', t_2) \mathrm{d}\mathbf{x}_0 \mathrm{d}t'', \end{aligned} \quad (2)$$

and initialization

$$M_0(\mathbf{x}_0', \mathbf{x}_0'', t, t_2) = -(H(t + t_2 - \varepsilon) - H(t + \varepsilon)) \times R(\mathbf{x}_0', \mathbf{x}_0'', -t), \quad (3)$$

where R_t denotes the retrieved data set without internal multiple reflections at time t_2 and H indicates the Heaviside function, which is used to apply the offset independent truncation window $(\varepsilon, t_2 - \varepsilon)$ in the equations. The constant ε indicates a small positive value, which can be taken as the half source time duration in practice. The initialization of the scheme (with M_0) is the time-reversed shot record at shot position $\mathbf{x}_0''$ for times between $(\varepsilon, t_2 - \varepsilon)$. The R_t in the left side of equation 1 is the same shot record, but without internal multiples. We follow Zhang and Staring (2018) and make time t_2 constant and independent of the source and receiver positions in the reflection response. Note that the integration is carried out over the receiver coordinate for both integrals, the same as implemented in the source code. The second term in the right side of equation 1 predicts all of the internal multiple reflections correctly. Equation 3 indicates that the measured reflection response is the only input of the MME scheme given in equation 1. To retrieve a data set without internal multiple reflections for all times t, this process must be repeated for all times t_2.

Equation 2 contains the terms that correct for the internal multiples that are present in $R(\mathbf{x}_0', \mathbf{x}_0'', t)$. To better explain the right side of equation 2, we divide the expression into two parts:

$$M_{2m}(\mathbf{x}_0',\mathbf{x}_0'',t,t_2)=\int_{t'=0}^{+\infty}\int_{\partial\mathbb{D}_0}R(\mathbf{x}_0''',\mathbf{x}_0',t')H(t-t'-\varepsilon)\times M_{2m-1}(\mathbf{x}_0''',\mathbf{x}_0'',t-t',t_2)\mathrm{d}\mathbf{x}_0'''\mathrm{d}t', \quad (4)$$

$$M_{2m-1}(\mathbf{x}_0''',\mathbf{x}_0'',t-t',t_2)=\int_{t''=0}^{+\infty}\int_{\partial\mathbb{D}_0}R(\mathbf{x}_0,\mathbf{x}_0''',t'')H(t'-t+t_2-t''-\varepsilon)\times M_{2(m-1)}(\mathbf{x}_0,\mathbf{x}_0'',t-t'+t'',t_2)\mathrm{d}\mathbf{x}_0\mathrm{d}t''. \quad (5)$$

Equation 4 is a time-domain *convolution* of R with M integrated over the spatial coordinate $\mathbf{x}_0'''$, which is the receiver position of the shot at $\mathbf{x}_0''$. Equation 5 is a time-domain *correlation* of R with M integrated over the spatial coordinate $\mathbf{x}_0$, which is the receiver position of the shot at $\mathbf{x}_0'''$. The Heaviside function in equation 4 is to exclude negative times for $t-t'<\varepsilon$ and only use the causal time in M_{2m-1}. In equation 5, the function $M_{2(m-1)}$ contains nonzero values for times larger than $t_2-\varepsilon$. These times should not contribute to the integral, and the Heaviside function guarantees that $M_{2(m-1)}$ does not have a contribution to the integration result for values of $t''+t-t'>t_2-\varepsilon$. Note that equations 4 and 5 perform very similar operations (they differ by a sign change) and are implemented by a single function. To evaluate equation 2, this function is applied two times. The convolution terms are the even-numbered operations with this function, and the correlation terms are the odd-numbered operations.

To better explain the method and for illustration purposes, the summation of the even M terms in equation 4 is defined as the field:

$$k_{1,i}^{-}(\mathbf{x}_0',\mathbf{x}_0'',t,t_2)=R(\mathbf{x}_0',\mathbf{x}_0'',t,t_2)-\sum_{m=1}^{i}\int_{t'=0}^{+\infty}\int_{\partial\mathbb{D}_0}R(\mathbf{x}_0''',\mathbf{x}_0',t')H(t-t'-\varepsilon)\times M_{2m-1}(\mathbf{x}_0''',\mathbf{x}_0'',t-t',t_2)\mathrm{d}\mathbf{x}_0'''\mathrm{d}t'. \quad (6)$$

We can evaluate equation 6 also for $t\geq t_2-\varepsilon$ and the equation can be further split in the time domain as follows:

$$k_{1,i}^{-}(\mathbf{x}_0',\mathbf{x}_0'',t,t_2)=\begin{cases}v_{1,i}^{-}(\mathbf{x}_0',\mathbf{x}_0'',t,t_2) & t<t_2-\varepsilon\\ u_{1,i}^{-}(\mathbf{x}_0',\mathbf{x}_0'',t,t_2) & t\geq t_2-\varepsilon\end{cases}, \quad (7)$$

where u_1^{-} and v_1^{-} are similar to the projected Green's function and focusing function in the regular Marchenko scheme as defined in Van der Neut and Wapenaar (2016). The minus superscript in equations 6 and 7 refers to upgoing wavefields at the receiver location $\mathbf{x}_0'$. To solve for M in equations 1 to 3, k_1^{-} is not needed. The time values in M between ε and $t_2-\varepsilon$ are used to solve the Marchenko equations and compute a value at t_2 in u_1^{-}. The solution for time t_2 in the MME scheme is collected from u_1^{-} at $t=t_2$.

Similarly for the summation of the terms in equation 5, a downgoing function is defined as

$$v_{1,i}^{+}(\mathbf{x}_0''',\mathbf{x}_0'',t,t_2)=\sum_{m=1}^{i}\int_{t''=0}^{+\infty}\int_{\partial\mathbb{D}_0}R(\mathbf{x}_0,\mathbf{x}_0''',t'')H(t'-t+t_2-t''-\varepsilon)\times M_{2(m-1)}(\mathbf{x}_0,\mathbf{x}_0'',t+t'',t_2)\mathrm{d}\mathbf{x}_0\mathrm{d}t'', \quad (8)$$

where v_1^{+} is similar to the projected focusing function in the regular Marchenko scheme as defined in Van der Neut and Wapenaar (2016). In v_1^{+}, the multiple annihilator is created, and this is demonstrated in the "Numerical examples" section. Equation 8 only holds for $\varepsilon<t<t_2-\varepsilon$. The plus superscript in equation 8 refers to downgoing wavefields. To solve the MME Marchenko equations, v_1^{+} is not needed and is only defined for illustration purposes to explain the mechanism of the method.

Time t_2 is the instant two-way traveltime in which the solution of the Marchenko equation is computed. The primary reflection is collected from u_1^{-} for every time instant t_2. This is a computationally expensive way because only one sample is collected in the output. Nevertheless, this process is fully automated and implemented without any human interaction or model information. It is possible to collect more than one sample around the instant time t_2 and to take bigger time steps, but the number of samples to use around t_2 must take into consideration the frequency bandwidth of the data. This statement is supported by examples in the detailed discussion of the implementation and allows the implementation of a faster algorithm.

In this MME scheme, the primary is collected from the original reflection data. The Marchenko scheme removes all overlapping internal multiples from earlier reflections, and the primary is untouched and keeps the physical reflection amplitude as present in the data.

T-MME

Internal multiple reflections and transmission losses in primary reflections can be accounted for by the T-MME scheme (Zhang et al., 2019). The equation is given by

$$R_r(\mathbf{x}_0',\mathbf{x}_0'',t=t_2)=R(\mathbf{x}_0',\mathbf{x}_0'',t=t_2)+\sum_{m=1}^{\infty}\bar{M}_{2m}(\mathbf{x}_0',\mathbf{x}_0'',t=t_2,t_2), \quad (9)$$

with

$$\bar{M}_{2m}(\mathbf{x}_0',\mathbf{x}_0'',t,t_2)=\int_{t'=0}^{+\infty}\int_{\partial\mathbb{D}_0}R(\mathbf{x}_0''',\mathbf{x}_0',t')H(t-t'+\varepsilon)\mathrm{d}\mathbf{x}_0'''\mathrm{d}t'\times\int_{t''=0}^{+\infty}\int_{\partial\mathbb{D}_0}R(\mathbf{x}_0,\mathbf{x}_0''',t'')H(t'-t+t_2-t''+\varepsilon)\bar{M}_{2(m-1)}(\mathbf{x}_0,\mathbf{x}_0'',t-t'+t'',t_2)\mathrm{d}\mathbf{x}_0\mathrm{d}t'' \quad (10)$$

and

$$\bar{M}_0(\mathbf{x}_0',\mathbf{x}_0'',t,t_2)=-(H(t+t_2+\varepsilon)-H(t+\varepsilon))R(\mathbf{x}_0',\mathbf{x}_0'',-t), \quad (11)$$

where R_r denotes the retrieved data set without internal multiple reflections and transmission losses in primary reflections. The trun-

cation window in equation 10 is different from the window in equation 2, which guarantees that the second term in the right side of equation 9 predicts the internal multiple reflections and transmission losses in primary reflections. In equation 10, the Heaviside function guarantees that $\bar{M}_{2(m-1)}$ does not have a contribution for values of $t'' + t - t' > t_2 + \varepsilon$. In contrast to equation 5, time t_2 is now part of the integration and is included in the sum of $\bar{M}_{2m}$. Still, as given in equation 11, the measured reflection response is the only input to solve the T-MME scheme given in equation 9.

The primary reflection is, different than in the MME scheme, collected from $\bar{v}_1^-$, which achieves the transmission compensation. There is no need to define $\bar{k}_1^-$ because $\bar{v}_1^-$ is already part of $\bar{M}_{2m}$. The scheme is applied for every time instant t_2 and has the same advantages and disadvantages as the MME scheme. In the T-MME scheme, the amplitude of the primary is automatically transmission compensated because it is the only way to predict and attenuate internal multiples from earlier primary reflections. We will return to this remark in the explanation of Figure 1.

The MME and T-MME schemes require only the measured reflection response R as input. The reflection response R needs to be deconvolved for the source-wavelet, and the free-surface-related multiple reflections must be removed. The output of a surface-related multiple elimination (Verschuur et al., 1992) scheme can meet these requirements. Diffracted and refracted waves are beyond the capability of both schemes, and a detailed analysis about these limitations can be found in Zhang et al. (2019).

MARCHENKO ALGORITHM

The basic Marchenko algorithm (MME) is explained in Algorithm 1. The arrays in this algorithm are stored in C-order; the last (right-most) addressed dimension is contiguous in memory. The discrete dimensions of these arrays are within square brackets $[\dots]$, and the arguments of function calls are within regular brackets $(\dots)$. The only data input of the algorithm is the measured reflection data R. These reflection data must be properly preprocessed as explained in Brackenhoff et al. (2019). The preprocessing must take care of the following:

1) Elimination of free-surface multiples. Note that there is also a very similar Marchenko algorithm that takes into account free-surface multiples as well. Ravasi (2017) discusses a redatuming algorithm similar to Singh et al. (2015) and requires a smooth model of the medium, whereas Zhang and Slob (2019) remove all multiples and do not need any model information.
2) Sufficient (i.e., alias-free) sampling in the spatial receiver and shot direction. Note that there are Marchenko-based methods that can fill in missing shotpoints or receiver locations, under the assumption that the available data are unaliased (Wapenaar and van IJsseldijk, 2020).
3) Compensation for dissipation.
4) Shot amplitude regularization.
5) Deconvolution for the source wavelet.

Following Algorithm 1, the preprocessed reflection data are read from the disk, transformed (by fast Fourier transform [FFT] operator $\mathcal{F}\{\dots\}$) to the frequency (ω) domain, and all shots and receivers are stored into the memory. This is the first step in the algorithm and the only significant data read. One single shot record (with shot number j), from which we want to suppress the internal multiples, is selected from this reflection data in the next step. This shot record is transformed back to time, time reversed (R^*), and stored in array DD. The first loop in the algorithm loops over the selected number of time samples that are processed to attenuate internal multiples. Typically, this represents all samples in the shot record, with a possible exclusion of the number of samples to the first reflection event in the selected shot record. For each time sample ii, the iterative Marchenko algorithm is executed. The largest difference from the algorithm described in Thorbecke et al. (2017) is that time-truncation along the first arrival time (from a focal point in the subsurface) is replaced by a constant time-truncation and the computation of a first arrival time is not needed anymore. The initialization of the algorithm by M_0 is from the same shot record j from which we would like to attenuate the internal multiples (DD). The term M_0 is a copy of the time-reversed shot record (see equation 3) and is set to zero from the first sample 0 to sample $n_t - ii + n_\varepsilon$, where n_t is the total number of samples in the shot record. The extra samples of n_ε take into account the time duration of the wavelet to exclude a possible reflection event at time ii. The initialization of $k_{1,0}^-$ is a complete (no time muting is carried out) copy of the shot record that still contains all of the internal multiples that we would like to remove.

With these two initializations, the iterations of the Marchenko algorithm can start. In each iteration, an updated field is computed by the integration of M_i with R. This integration process is called synthesis, produces the output RM_i, and is explained in more detail below. Depending on the iteration number i, being odd or even, different time muting windows are in use to mute

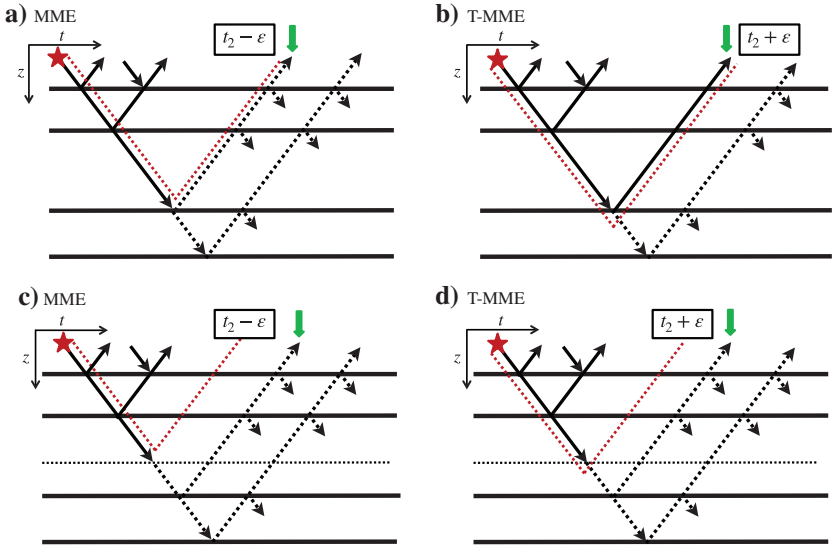

Figure 1. Comparison of the MME and T-MME schemes. (a and b) A selected time t_2 equal to the two-way traveltime of the third reflector. The time-truncation window is indicated with a red dotted line. The dotted lines are events that are excluded in M_i, and the solid lines are events included in M_i, after application of the time window. (c and d) A time between two reflectors.

events in RM_i and to compute an updated M_{i+1}. For even iterations, the times between $ii - n_\varepsilon$ and n_t are set to zero, and, for odd iterations, the times between 0 and $ii + n_\varepsilon$ are set to zero. Only in the odd iterations is $k^-_{1,i}$ updated with the unmuted M_{i+1}. In this update of $k^-_{1,i}$, internal multiples around time ii are attenuated. This is the update represented in equation 1, where the update M_{2m} is in fact one even and one odd iteration in the implemented Marchenko algorithm and, hence, the notation with $2m - 1$ in equation 6.

In the regular redatuming Marchenko algorithm (Thorbecke et al., 2017), the truncation windows follow the first arrival time of a focal point in the subsurface. In the MME algorithm, the focal point is projected on the surface and the time-truncation is conveniently chosen at a constant time. The flat time window has the big advantage that it requires no additional model or data information. Meles et al. (2020) demonstrate that, in the application of the multiple elimination algorithm to dipping plane waves, a time truncation consistent with the dip angle must be used.

Depending on the position of strong reflectors, typically, 10–50 Marchenko iterations are needed for each time sample ii in the selected shot record. The presence of strong reflectors in the shallow part makes the convergence slow at large time instances; see also Figure 8. The reason is that higher order multiples are attenuated with events that are created in v^-_1 and that are removed again later when the first-order multiple is finally removed by a converged multiple attenuator. When the first-order multiple is removed, all multiples are removed; hence, all earlier higher order multiple attenuator artifacts will also vanish. Once the iterations are finished, the output of sample ii of the updated Marchenko result u^-_1 is stored in sample ii in the multiple free shot record R_t and the final output of the program that represents the selected shot record with attenuated internal multiples. It is a computationally intensive task to solve the Marchenko equations for each sample ii in the shot record. Algorithm 2 is a faster (10–20x) implementation of Algorithm 1.

In Algorithm 2, after the Marchenko equations are solved at time sample $ii - 1$, the next time sample ii is initialized with the result of time sample $ii - 1$ (Zhang and Slob, 2020b). The idea is that to remove the internal multiples at the next time sample there is no need to start from scratch and remove the multiples that were already removed in the previous time sample. For every next time sample, all earlier attenuated multiples need to be attenuated plus one (or a few) more. In the Marchenko update for the new time sample, only the multiples that were not removed previously need to be removed. This is a small deviation from the previous results, and usually two iterations are sufficient to accomplish the update for

Algorithm 1. The basic Marchenko algorithm, without transmission loss compensation, as implemented in the provided source code. Integer time sample number *it*, which runs from *i*start to *i*end, represents time $t = it * \Delta t$. The number of recorded time samples is n_t, the time duration of the source signature $\varepsilon = n_\varepsilon * \Delta t$, and time sample *ii* represents instant time $t_2 = ii * \Delta t$. The number of receivers in R is $N_{\mathbf{recv}}$, and the number of shots is $N_{\mathbf{shots}}$. The *i* loop represents the number of Marchenko iterations n_i. Note that the sample expression $n_t - it$ stands for negative time $-t$.

Main **begin**
  Read SU-style input parameters
  Initialization, reading of input parameters, and allocate arrays
  READ($R[N_{\text{shots}}, i\omega, N_{\text{recv}}]$)
  $DD[N_{\text{recv}}, it] = \mathcal{F}^{-1}\{R^*[j, i\omega, N_{\text{recv}}]\}$
  for $ii \leftarrow i$start **to** $i$end **do**
    $M_0[N_{\text{recv}}, it] = \begin{cases} 0 & 0 < it < n_t - ii + n_\varepsilon \\ -DD[N_{\text{recv}}, it] & n_t - ii + n_\varepsilon \le it < n_t \end{cases}$
    $k^-_{1,0}[N_{\text{shots}}, it] = DD[N_{\text{recv}}, n_t - it]$
    $v^+_{1,i}[N_{\text{shots}}, it] = 0$
    for $i \leftarrow 0$ **to** n_i **do**
      synthesis(R, M_i, RM_i)
      $M_{i+1}[N_{\text{shots}}, it] = RM_i[N_{\text{shots}}, n_t - it]$
      if (i % 2 == 0) **then**
        $M_{i+1}[N_{\text{shots}}, it] = 0; \quad ii - n_\varepsilon < it < n_t$
        $v^+_{1,i+1}[N_{\text{shots}}, it] = v^+_{1,i}[N_{\text{shots}}, it] + M_{i+1}[N_{\text{shots}}, it]$
      else
        $k^-_{1,i+1}[N_{\text{shots}}, it] = k^-_{1,i}[N_{\text{shots}}, it] - M_{i+1}[N_{\text{shots}}, n_t - it]$
        $M_{i+1}[N_{\text{shots}}, it] = 0; \quad 0 < it < n_t - ii + n_\varepsilon$
      end
    end
    $R_t[j, N_{\text{shots}}, ii] = k^-_{1,n_i}[N_{\text{shots}}, ii]$
  end
end

Algorithm 2. Faster Marchenko algorithm that uses previous results from time instant $ii - 1$ ($k^{-,(ii-1)}_{1,n-1}$,) as input for the current time instant *ii*.

Main **begin**
  Read SU-style input parameters
  Initialization, reading of input parameters, and allocate arrays
  READ($R[N_{\text{shots}}, i\omega, N_{\text{recv}}]$)
  $DD[N_{\text{recv}}, it] = \mathcal{F}^{-1}\{R^*[j, i\omega, N_{\text{recv}}]\}$
  for $ii \leftarrow i$start **to** $i$end **do**
    $k^-_{1,0}[N_{\text{shots}}, it] = k^{-,(ii-1)}_{1,n_i}[N_{\text{shots}}, it]$
    $M_0[N_{\text{shots}}, it]$
    $= \begin{cases} 0 & 0 < it < n_t - ii + n_\varepsilon \\ DD[N_{\text{shots}}, n_t - it] - k^-_{1,0}[N_{\text{shots}}, n_t - it] & n_t - ii + n_\varepsilon \le it < n_t \end{cases}$
    for $i \leftarrow 0$ **to** n_i **do**
      synthesis(R, M_i, RM_i)
      $M_{i+1}[N_{\text{shots}}, it] = RM_i[N_{\text{shots}}, n_t - it]$
      if (i % 2 == 0) **then**
        $M_{i+1}[N_{\text{shots}}, it] = 0; \quad ii - n_\varepsilon < it < n_t$
      else
        $M_{i+1}[N_{\text{shots}}, it] = M_{i+1}[N_{\text{shots}}, it] - DD[N_{\text{recv}}, it]$
        $k^-_{1,i+1}[N_{\text{shots}}, it] = -M_{i+1}[N_{\text{shots}}, n_t - it]$
        $M_{i+1}[N_{\text{shots}}, it] = 0; \quad 0 < it < n_t - ii + n_\varepsilon$
      end
    end
    $R_t[j, N_{\text{shots}}, ii] = k^-_{1,n_i}[N_{\text{shots}}, ii]$
  end
end

the next time sample. The initial M_0 in the fast algorithm is the difference between the original data (DD) and $k^{-,(ii-1)}_{1,n-1}$; the already estimated internal multiples from time sample $ii-1$. The initial $k^{-}_{1,0}$ is the previous result $k^{-,(ii-1)}_{1,n-1}$. With these initializations, the update term RM_i contains only a small correction because it is based on a converged previous result that is very close to the actual solution. To get the complete internal multiple in M_{i+1}, DD is added to RM_i (Zhang and Slob, 2020b).

In this fast algorithm, only one pair of even-odd iterations is needed to reach convergence. In principle, we could solve the equations only one time and use that result to update all other time samples. On simple models of numerically modeled data, this works fine indeed. However, on geologically complicated models of numerically modeled data and on field data, we have to do a full update every 10–20 recursive updates and the speed-up of the faster algorithm is limited to one order of magnitude. On complex data sets, we would advise beginning with the basic algorithm and then verifying if the fast algorithm can be used to speed up the computations. The reason for this limited use of the fast algorithm is that, for complex data sets and a large number of iterations, artifacts, for example, introduced by a limited aperture, can get amplified. The primary reflections will still converge, but numerical artifacts are not accounted for in the algorithm and can diverge. In the iterative scheme, each update adds two iterations to the already computed result based on, for example, 30 iterations. With 10 iterative updates, 20 iterations are added and can cause artifacts being amplified to signal level.

Algorithm 3. Marchenko synthesis kernel with $i\omega = i * \Delta\omega \left(= \frac{2\pi}{n_t * \Delta t}\right)$.

Synthesis($R[N_{\text{shots}}, i\omega, N_{\text{recv}}), M[N_{\text{shots}}, it], RM[N_{\text{shots}}, it]$)
begin
  $Fop[i\omega, N_{\text{shots}}] = \mathcal{F}\{M[N_{\text{shots}}, it]\}$
  $RM[N_{\text{shots}}, t] = 0$
  #pragma omp parallel for
  for $k \leftarrow 0$ **to** N_{shots} **do**
    for $i\omega \leftarrow \omega_{\text{min}}$ **to** ω_{max} **do**
      for $i \leftarrow 0$ **to** N_{recv} **do**
        $\text{sum}[i\omega] = \text{sum}[i\omega] + R[k, i\omega, i] * Fop[i\omega, i]$
      end
    end
    $RM[k, it] = \mathcal{F}^{-1}\{\text{sum}[i\omega]\}$
  end
End

In the algorithm, we solve the Marchenko equations for each sample ii. From the theory, we know that the first event after sample ii is a primary reflector (all multiple reflections generated by the reflectors before sample ii are removed by the scheme). Hence, a few samples after sample ii will still be free of internal multiples. We could make larger steps with ii and use the Marchenko result for several samples (at least n_ε samples because that is the time resolution with which we already are working) after sample ii. This can speed up the code by n_ε (typically 20) times. This is similar to the fast algorithm, but without making any iterations and directly using the previous computed result.

The synthesis process shown in Algorithm 3 computes the second integrant in the right side of equation 2. The synthesis function is a straightforward matrix-vector multiplication. The reflection data are stored in such a way that the innermost loop, which sums over the receiver positions within a shot, is contiguous in memory. To speed up the computation, a parallel OpenMP region is carried out over the outer N_{shots} loop. An alternative implementation of the synthesis process is to make the frequency loop the outer loop and use a BLAS dgemv function to compute the matrix-vector multiplication. This implementation also will be efficient when all shots are computed at the same time and the BLAS matrix-matrix dgemm function becomes the kernel of the synthesis process. Note that in the synthesis process, the integration is carried out over the number of receivers per shot and each integration result is stored at the shot position. Thus, after the synthesis process N_{shots} output traces are computed.

From a computational point of view, the transmission-compensated algorithm (T-MME) is the same as the MME algorithm, except for the application of the time-truncation window. The sample length of the wavelet (n_ε) is applied in the opposite time direction for the T-MME algorithm. The extra samples of n_ε in the MME algorithm take into account the length of the wavelet to exclude a possible event at instant time ii in the initialization and update of M_i. Suppose that time ii is the two-way traveltime of a reflector (see Figure 1a). The reflection of

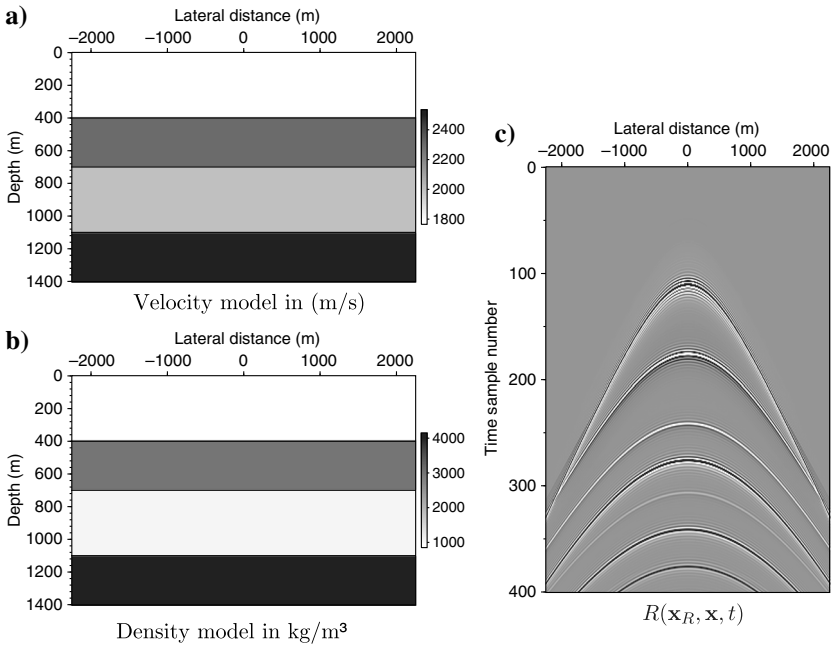

Figure 2. Four layer model with (a) velocity and (b) density parameters. (c) A shot record, with source position $\mathbf{x} = (x = 0, z = 0)$ and receivers at $\mathbf{x}_R = (x = x_r, z = 0)$; the source wavelet in R has a flat frequency spectrum from 5 to 90 Hz.

the reflector is excluded in M_i in the MME algorithm (Figure 1a), but it is included in $\bar{M}_i$ in the T-MME algorithm (Figure 1b). In the T-MME algorithm, the reflected event at instant time ii ends up in the updated $\bar{v}_1^-$, whereas in the MME algorithm the reflected event from the original shot record ends up in u_1^-. When the instant time ii is chosen between two reflectors, there is no difference between the updates made in the MME (Figure 1c) or T-MME (Figure 1d) scheme.

To get to the T-MME scheme from Algorithm 1, one has to replace in the defined time windows $+n_\varepsilon$ with $-n_\varepsilon$. Then, R_t becomes R_r that contains the transmission-compensated primary reflections.

NUMERICAL EXAMPLES

The Marchenko algorithm is illustrated with a 1.5D horizontally layered model shown in Figure 2. The numerical modeling is carried out with a finite-difference modeling program (Thorbecke and Draganov, 2011) that is also included in the software package. The input source signature, to model the reflection response $R(\mathbf{x}'_0, \mathbf{x}''_0, t)$, is approximately a sinc-function with a flat spectrum of amplitude one between $f_{\min}$ and $f_{\max}$ (5–90 Hz) to represent a deconvolved source wavelet. In the finite-difference program for modeling $R(\mathbf{x}'_0, \mathbf{x}''_0, t)$, a source of vertical force is chosen. The receivers are placed at $z = 0$ and measure the pressure field. A fixed spread acquisition is chosen between −2250 and 2250 m, and the distance between the 901 source/receiver positions is 5 m. The receiver traces have a time sampling interval of 4 ms and 1024 recorded time samples.

The first iterations

Figure 3 demonstrates the first iteration of equation 5 with $m = 1$ to compute M_1 for time sample number 276 (t = 1.100 s) from M_0. Time sample 276 corresponds to the zero-offset arrival time of the third reflector. In this first step, all shots in the reflection data R are correlated with a time-windowed shot record. In our example, we use the middle shot record; $R_0(\mathbf{x}_R, \mathbf{x} = (0, 0), t)$ (shot number $j = 451$). Before the correlation is carried out, the selected shot record is first set to zero beyond time sample $276 - n_\varepsilon$, multiplied by −1 and time reversed, at which moment we have $M_0(t)$ in equation 3. In Figure 3b, the shot record is convolved with a Ricker wavelet to reduce the ringing of the flat spectrum of the (deconvolved) wavelet present in R (Figure 3a). The number of n_ε (in this example $n_\varepsilon = 20$) samples excludes the reflection from the third reflector in M_0. In Figure 3, the middle shot record of R (Figure 3a, where we used source receiver reciprocity) is correlated with the time windowed $M_0(-t)$ (Figure 3b) to give the result in Figure 3c. The events in Figure 3b include the first and second reflections and the first internal multiple between the first and second reflectors. In the correlation result (Figure 3c), we see the autocorrelation of the three reflection events around $t = 0$ (with events at negative times appearing at the bottom of the panel). Note that the long train of events starting at the positive time axis in Figure 3c can interfere with events at the end of the time axis. To overcome this time interference, we usually pad the time axis with zeros before the transformation to the frequency domain where the correlation is computed.

The correlation result is time reversed and is shown in Figure 3d for the first 400 samples. There are only three events in Figure 3d, and these originate from correlation with the three events in Figure 3b with the first three events ($\mathbf{r}_1, \mathbf{r}_2, \mathbf{m}_1$) in the shot record. According to the integral in equation 5, to obtain an output trace of M_1 the traces in Figure 3d are summed together. The stationary points of the events in Figure 3d give a contribution in the result of the summation. Besides the stationary points, truncated events (in time and space) give unwanted contributions that show up as artifacts in the final result.

The integration result is set to zero for samples larger than $276 - n_\varepsilon$ and ends up as a trace at position zero (the middle trace) of M_1 shown in Figure 3e. In Figure 3e, the truncation appears to be

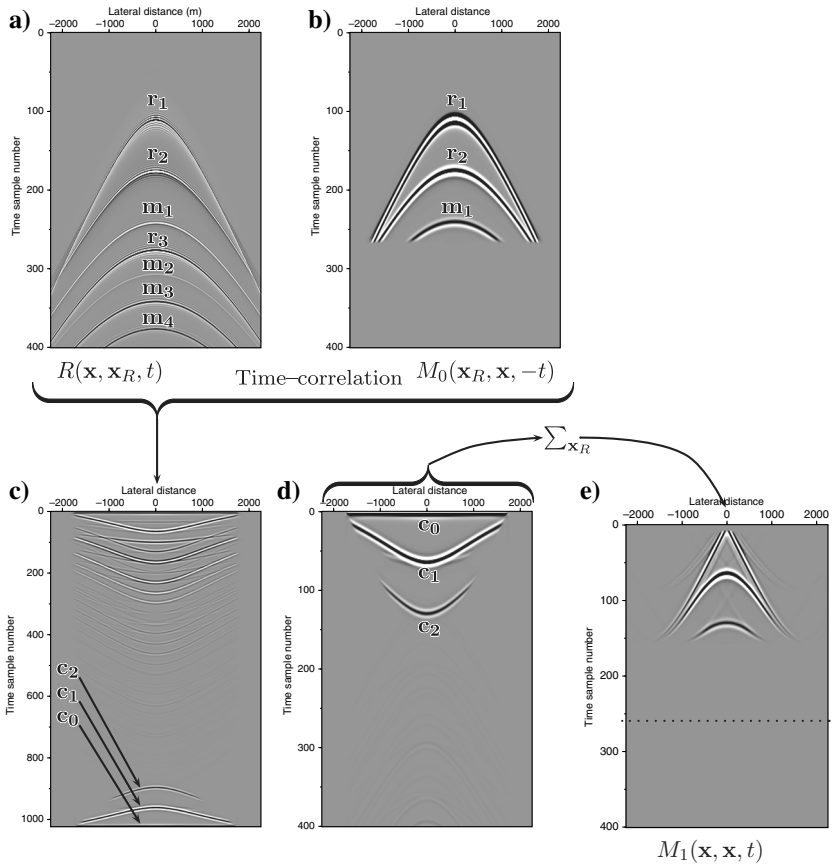

Figure 3. Computational steps to compute M_1 from M_0 at time sample number 276. The middle shot record from R is shown in (a); time truncated after sample $276 - n_\varepsilon$, and convolved with a Ricker wavelet, it gives M_0 in (b). Time correlation of (a) with (b) gives (c). After time reversal of (c) and applying the time window again gives (d). The traces in (d) are summed together, and only the stationary point of events above sample $276 - n_\varepsilon$ will end up in the middle trace of M_1 (e). The mute window n_ε samples later than $t = 0$ are needed to mute the autocorrelation of the first event. The labeled events $\mathbf{r}_i$ indicate the ith reflector and $\mathbf{m}_l$ the lth multiple. (c) The labeled correlated events are $\mathbf{c_0} = \mathbf{r}_1^*.\mathbf{r}_1 + \mathbf{r}_2^*.\mathbf{r}_2 + \mathbf{m}_1^*.\mathbf{m}_1$, $\mathbf{c_1} = \mathbf{r}_2^*.\mathbf{r}_1 + \mathbf{m}_1^*.\mathbf{r}_2$, and $\mathbf{c_2} = \mathbf{m}_1^*.\mathbf{r}_1$.

at sample 160, but that is the truncation in Figure 3b shifted upward in time with the arrival time of the first reflector. The truncation at sample $276 - n_\varepsilon$ is indicated with a dotted line. There are two hyperbolic events visible and a few linear artifacts. The first hyperbolic event originates from correlation of events $\mathbf{r}_2^*.\mathbf{r}_1$ and events $\mathbf{m}_1^*.\mathbf{r}_2$, and the second hyperbolic event from the first internal multiple and first reflector $\mathbf{c}_2 = \mathbf{m}_1^*.\mathbf{r}_1$. The linear events are unwanted artifacts due to truncation and can be suppressed by applying a smooth taper at the truncation boundaries in time and space.

Figure 4 demonstrates the computation of the second iteration to compute M_2 from M_1 (Figure 3e) according to equation 4 with $m = 1$. The reflection data (Figure 4a) are convolved with M_1 (Figure 4b) that contains three main events: a linear artifact ($\mathbf{a}_1$) and two correlation results ($\mathbf{c}_1$ and $\mathbf{c}_2$). Convolving M_1 with the middle shot record of the data R gives Figure 4c. The hyperbolic events in M are now back at the same times as the reflection events in the shot record. The linear artifacts in M_1 also convolve with all events in R and introduce many (mostly linear) artifacts. The convolution result is reversed in time (Figure 4d), and, after the integration in equation 4 over the lateral coordinate $\mathbf{x}_R$, it becomes the middle trace in M_2 (Figure 4e). Most of the linear artifacts are reduced in amplitude due to the destructive interference in the integration, only the "$\mathbf{a}_2 = \mathbf{r}_1.\mathbf{a}_1$" artifact is still present in M_2. The first term in the sum in equation 1 is now computed: M_2. The last events in the time reverse of M_2, presented in Figure 4e, will already attenuate the multiple event $\mathbf{m}_1$ in the shot record.

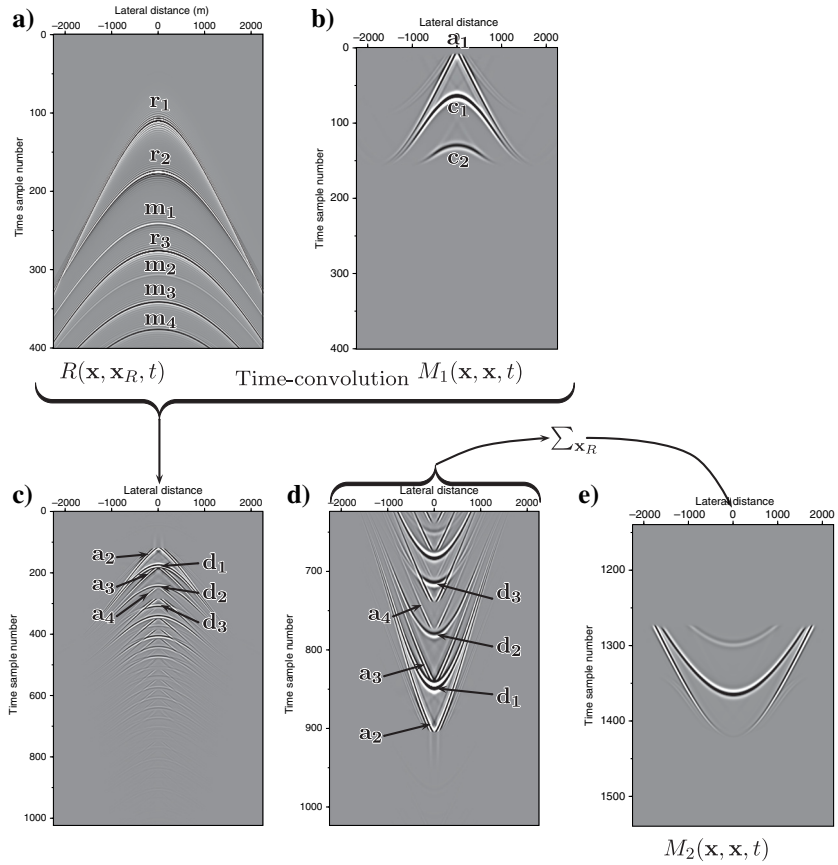

Figure 4. Computational steps to compute $M_2(\mathbf{x}, \mathbf{x}, t)$ from M_1 at time sample number 276. The middle shot record from R is shown in (a) and M_1 truncated after sample 276 (and computed in Figure 3e) in (b). Time convolution of (a) with (b) gives (c). After time reversal of (c) and applying the time window again gives (d). The traces in (d) are summed together, and only stationary events later than sample $n_t - 276 + n_\varepsilon$ end up in the middle trace of M_2 (e). The labeled events $\mathbf{r}_i$ indicate the ith reflector, $\mathbf{m}_l$ is the lth multiple, and $\mathbf{a}_n$ is the nth artifact. The labeled events from the convolution between (a) R and (b) M_1 are $\mathbf{a_2} = \mathbf{r_1}.\mathbf{a_1}, \mathbf{a_3} = \mathbf{r_2}.\mathbf{a_1}, \mathbf{a_4} = \mathbf{m_1}.\mathbf{a_1}, \mathbf{d_1} = \mathbf{r_1}.\mathbf{c_1}$, $\mathbf{d_2} = \mathbf{r_1}.\mathbf{c_2} + \mathbf{r_2}.\mathbf{c_1}$, and $\mathbf{d_3} = \mathbf{r_2}.\mathbf{c_2} + \mathbf{m_1}.\mathbf{c_1}$.

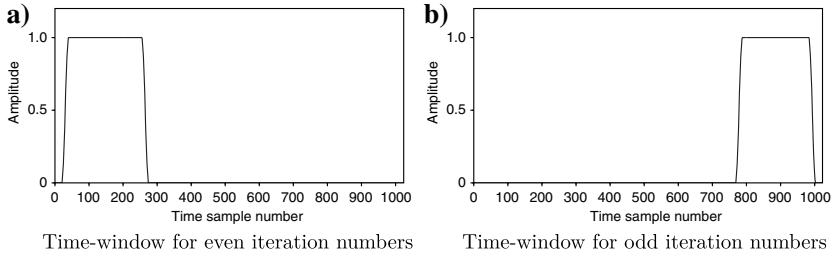

Figure 5. Time-window functions in the Marchenko scheme with a smooth cosine-shaped transition zone. This transition zone has a default setting of $0.5n_\varepsilon$ samples and is within the n_ε samples.

Time reverse of M_2, presented in Figure 4e, will already attenuate the multiple event $\mathbf{m}_1$ in the shot record.

To compute M_1 (in general, odd-numbered updates to M_i), events are shifted backward in time (correlation) with the times of the events in M_0. To compute M_2 (even-numbered updates to M_i) from M_1, events are shifted forward (convolution) in time. The even and odd iterations are treated differently in the scheme. Each even iteration updates M_i and v_1^+, and each odd iteration updates M_i and k_1^-. The scheme reverts the time axis for each iteration, hence, the time windows, which set time samples to zero, also switch. These time windows, for sample 276, are shown in Figure 5. In these time windows, a smooth cosine-shaped transition zone is used to reduce the time-truncation artifacts.

Multiple removal in action

The results in Figure 6 are partial solutions of the Marchenko equations computed for time sample $ii = 200$. After applying the time window, which sets all samples in M_0 to zero beyond $200 - n_\varepsilon$, there are no internal multiple reflections present anymore in M_0. The times between 0 and sample 200 include $\mathbf{r}_1$ and $\mathbf{r}_2$, but not $\mathbf{m}_1$; see Figure 3b. In the first iteration to compute v_1^+, according to equation 8, one extra event in v_1^+ (Figure 6a event $\mathbf{c}_1$) is created to correct for the amplitude of the second reflector in v_1^-. Note that the time windows in Figure 6a appear to be around sample 80, but this is the time window applied in M_0 shifted by the correlation to negative times and time reversed. The amplitude of this event $\mathbf{c}_1$ converges to the amplitude that can

annihilate the amplitude of the first multiple. Applying the converged v_1^+ on the reflection data through equation 4 causes all multiples arising from bounces between the first and second reflector to vanish from the data in equation 1. The scheme finishes without ever having "seen" the multiple; from $\mathbf{r}_1$ and $\mathbf{r}_2$ alone, it created an event that can attenuate all of the internal multiples between these reflectors. The arrows in Figure 6c, which shows $k^-_{1,30}(t)$ and is computed according to equation 6, point at the multiples that are already partly gone. The multiples are only partly removed because only a small offset range of $\mathbf{r}_2$ is used at sample 200. Repeating the scheme for samples larger than 200 will include larger offsets of $\mathbf{r}_1$ and $\mathbf{r}_2$ and also attenuate the higher offsets for all internal multiples between $\mathbf{r}_1$ and $\mathbf{r}_2$.

For the investigation of the amplitudes of the event in v_1^+, we assume, for the sake of argument, that the reflection coefficient is a constant. The primary reflections in Figure 3b have local reflection a_1, a_2 for, respectively, the events labeled $\mathbf{r}_1, \mathbf{r}_2$. We consider the situation in Figure 6, for time sample 200 that only creates one extra event in v_1^+. We demonstrate that, after sufficient iterations, the event in v_1^+ has converged to an amplitude that can cancel the first-order multiple and hence all higher order multiples related to that event. For sample 200, M_0 contains only the primary reflections $\mathbf{r}_1, \mathbf{r}_2$ that have amplitude:

$$r_1^a = a_1, \tag{12}$$

$$r_2^a = (1 - a_1^2)a_2. \tag{13}$$

Figure 7 is a sketch of the reflection paths and reflection and transmission coefficients for this two-reflector case. According to equation 5, for the first iteration M_0 is correlated with R and integrated over the receiver coordinate. After applying the time window on M_1 only one event remains: event $\mathbf{c}_1 = \mathbf{r}_2^*.\mathbf{r}_1$ in Figure 6a with the amplitude

$$c_{1,1}^a = a_1(1 - a_1^2)a_2. \tag{14}$$

The second subscript in $c_{1,1}^a$ indicates the iteration number. This event is convolved with R in the next iteration (according to equation 4), and, after time windowing, only one event $\mathbf{r}_1.\mathbf{c}_1$ remains at the time of the reflection of the second reflector with the amplitude

$$c_{1,2}^a = a_1^2(1 - a_1^2)a_2. \tag{15}$$

In each next iteration, alternating between equations 5 and 4, another multiplication with a_1 is added; in general, for iteration i, we have

$$c_{1,i}^a = (a_1)^i(1 - a_1^2)a_2. \tag{16}$$

Summation of all odd $c_{1,i}^a$ iterations i gives the final amplitude of the multiple annihilation event $\mathbf{c}_1$ in v_1^+. The initialization of v_1^+ is zero, and the summation of the odd terms leads to

$$\begin{aligned}\sum_{i=0}^{n_i} c_{1,1+2i}^a &= \sum_{i=0}^{n_i} (a_1)^{1+2*i}(1 - a_1^2)a_2 \\ &= a_1a_2 - a_1^3a_2 + a_1^3a_2 - a_1^5a_2 + a_1^5a_2 - a_1^7a_2 + \ldots \\ &\approx a_1a_2. \end{aligned} \tag{17}$$

Application of v_1^+ to the data creates multiple-free data in the resulting u_1^- and is shown in Figure 6c. The first-order internal multiple from the data and the multiple annihilation event $\mathbf{c}_1$ in Figure 6a, with amplitude a_1a_2, will meet each other in time just below the first reflector. At that point in time, the annihilator cancels the first-order downgoing internal multiple and, with that, all other related multiples. To be able to cancel the first downgoing internal multiple, the annihilator must have the same amplitude as that event. The first-order multiple event $\mathbf{m}_1$ in Figure 3b has the amplitude

$$m_1^a = -(1 - a_1^2)a_2^2a_1. \tag{18}$$

After convergence of the scheme, the multiple annihilator event $\mathbf{c}_1$ is convolved with the second reflector $\mathbf{r}_2$ of R in the next iteration and arrives at the same time as $\mathbf{m}_1$ and has the same amplitude as m_1^a:

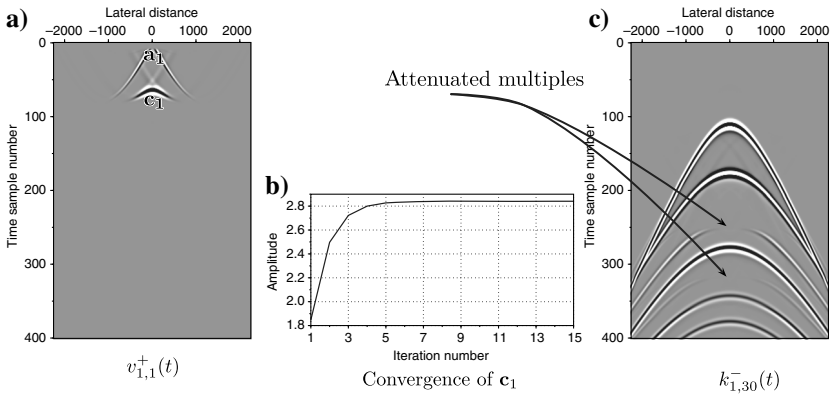

Figure 6. Creation of the event (labeled $\mathbf{c}_1$) that annihilates all of the internal multiples between the first and second reflectors; the artifact $\mathbf{a}_1$ is ignored in the analysis. (a) The $v_{1,1}^+(t)$ for the first Marchenko iteration at sample number $ii = 200$. (b) The convergence of the maximum amplitude in $\mathbf{c}_1$ is shown as a function of the iteration count. (c) The annihilated multiples in $k^-_{1,30}(t)$ after 30 iterations.

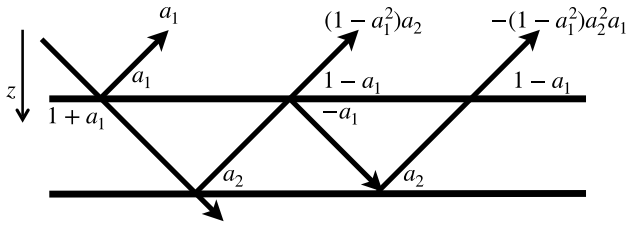

Figure 7. Sketch of the raypaths and reflection and transmission coefficients in a three-layer constant-velocity and variable-density model. The local reflection coefficients of the first and second reflector are a_1 and a_2, respectively.

$$c_1^{ar_2^a} = a_1 a_2 . r_2^a$$
$$= (1 - a_1^2) a_2^2 a_1. \quad (19)$$

This result is added to the data to cancel the internal multiple at $\mathbf{m}_1$ as shown in Figure 6c and equation 1. Furthermore, convolution of $\mathbf{c}_1$ with $\mathbf{m}_1$ will create the annihilator of the second-order multiple;

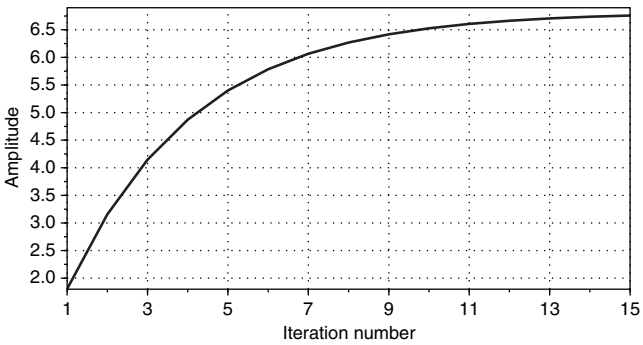

Figure 8. Convergence of the maximum amplitude of the event (labeled $\mathbf{c}_1$ in Figure 6a) that annihilates all the internal multiples between the first and second reflector in a high-contrast medium.

hence, $\mathbf{c}_1$ will automatically annihilate all higher order multiples as well.

To complete the amplitude analysis, the amplitude of the second reflector in $\bar{v}_1^-$ (from the equivalent of equation 7 for the T-MME scheme) can be computed according to equation 10 and is constructed from the even amplitude terms in equation 16. The initialization of $\bar{v}_1^-$ is the time reversed shot record (*DD* in Algorithm 1). Summation of all even $c_{1,i}^a$ iterations i at the time of the second reflector creates the final amplitude for the second reflector in $\bar{v}_1^-$:

$$a_2 = (1 - a_1^2) a_2 + \sum_{i=1}^{n_i} a_1^{2*i} (1 - a_1^2) a_2$$
$$= a_2 - a_1^2 a_2 + a_1^2 a_2 - a_1^4 a_2 + a_1^4 a_2 - a_1^6 a_2 + \ldots$$
$$\approx a_2. \quad (20)$$

This shows that the transmission-compensated local reflectivity can be collected from v_1^- as implemented in the T-MME scheme. The approximation sign is due to a limited number of iterations in the numerical implementation.

Figure 8 is obtained in the same way as Figure 6b, but with high-contrast layers. The velocity of the layers is the same as used in Figure 6, but the density contrast between the layers has been in-

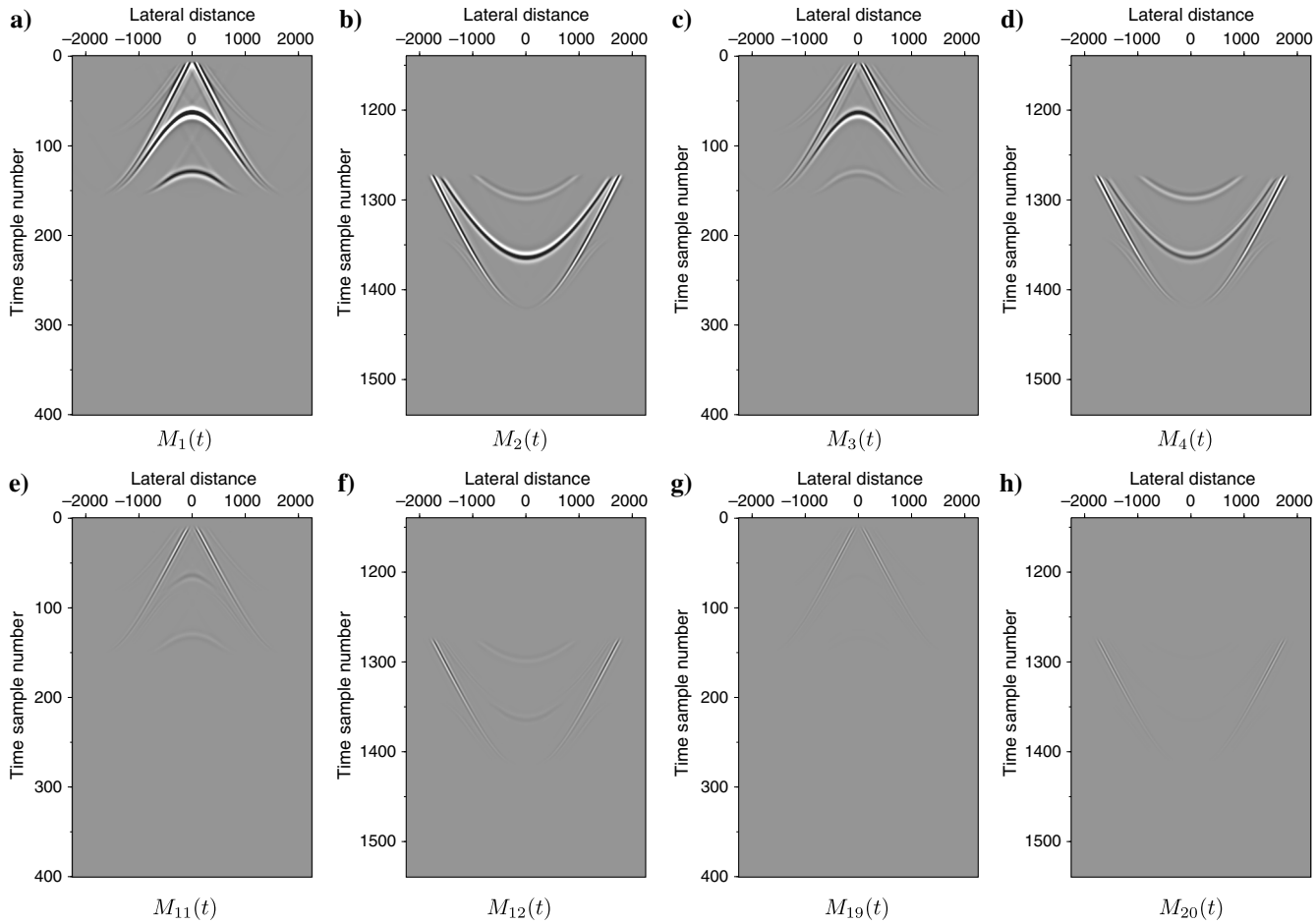

Figure 9. The term M_i fields for a focal time at sample $ii = 276$; the zero-offset arrival of the third reflector. All figures are plotted with the same clipping factor.

creased from a factor 3 (1000–3000) to 10 (500–5000). Compared to Figure 6b, the convergence is much slower in this high-contrast medium. In equation 17, the higher order terms will have larger values in high-contrast media and require more iterations for convergence.

Higher iteration counts

The first few iterations for the update terms M_i are shown in Figure 9. The truncation time is chosen at sample 276, and a first-order multiple of the second layer is present in the initialization shot-record M_0 after time truncation. For higher numbers of iterations, the update terms become smaller in amplitude, indicating that the scheme converges. All of the updates show the same number of events, and only the amplitude of the events changes during the iterations.

In the odd iterations, the function $k^-_{1,i}(t)$ (see equation 6) is updated with the odd $M_i(-t)$ terms and four selected iterations are shown in Figure 10. After two iterations, all order multiples are predicted, but with incorrect amplitudes. In the following iterations, the removal of higher order multiples is improved because the removal of the first-order multiple improves. After 20 iterations, the internal multiple events (indicated with arrows) have further attenuated and are not visible anymore; compare Figure 10b with 10h. The higher order multiples do not have to be removed by extra events in v_1^+, but they are removed automatically by removing the first-order multiple.

In Figure 10f, one can observe that the first internal multiple (pointed at by the top arrow) is already attenuated beyond sample $276 - n_\varepsilon + 1$, but it is not yet completely attenuated before sample $276 - n_\varepsilon$. The first $276 - n_\varepsilon$ samples belong to v_1^-, where the information on attenuation of the internal multiple is constructed, whereas samples from $276 - n_\varepsilon + 1$ onward belong to u_1^-, where the multiple is already attenuated. The constant-time cross section (for all lateral positions) in $k^-_{1,i}$ at sample 276 is stored in the final output R_t at sample 276. In the v_1^- part (between samples 1 and 276) of k_1^-, the second reflector has its local reflection coefficient as amplitude, whereas in the u_1^- part (from sample 276 onward) it has its physical amplitude with two-way transmission effects.

Different time instances

In Figure 11, the Marchenko equations are solved for different time samples ii and it is possible to investigate how k_1^- changes for larger sample numbers. It is observed that, not only at sample ii but also before and beyond ii, the events related to internal multiples are attenuated. Sample point 276 corresponds to the arrival time

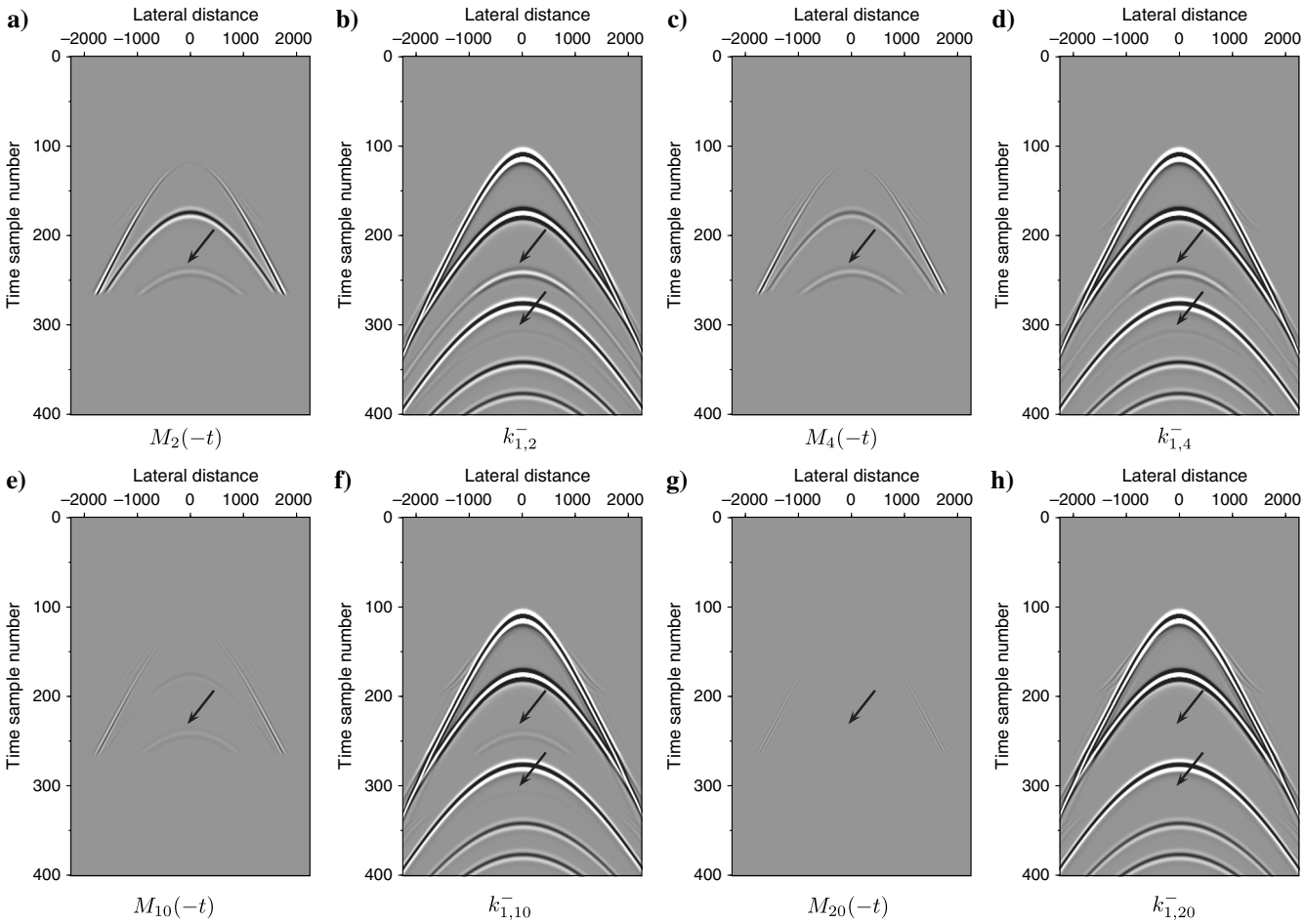

Figure 10. Updates for $k^-_{1,i}$ for a focal time at sample $t_2 = 276$ after i iterations. The arrow indicates the first- and second-order internal multiple between the first and second reflector.

of the third reflector. The times in Figure 11a–11d are all before sample 276, and we do not observe a change in the number of events. However, going from sample 246 (Figure 11a) to 276 (Figure 11d), one can see that the multiple, arriving in time between the second and third reflectors, gets more and more attenuated at larger and larger offsets. This also explains the success of the fast algorithm: to compute the solution in the next time sample, there is only a small change needed and a few iterations are sufficient to solve for the multiple attenuation at higher offsets. When the sample time ii passes the arrival time of the third reflector, a nonphysical event (pointed out by an arrow in Figure 11e–11h) appears just below the arrival time of the second reflector. This nonphysical reflector is the annihilator event in v_1^+ that compensates all internal multiples created between the second and third reflector. The cancelation of the internal multiples is observed at larger time samples (Figure 11e–11h); all internal multiples related to the third reflector are canceled out.

Figure 12a and 12b shows sketches of the situation in which the time instant ii corresponds to a depth above or below the third reflector, respectively. The event that compensates all internal multiples related to the second reflector (the green arrow in Figure 12a) coincides in traveltime with the reflection of the second reflector and also compensates for the transmission loss of the reflection from the second reflector. The internal multiples related to the third reflector are compensated by the red-arrow event (Figure 12b) which coincides with the reflection time of the third re-

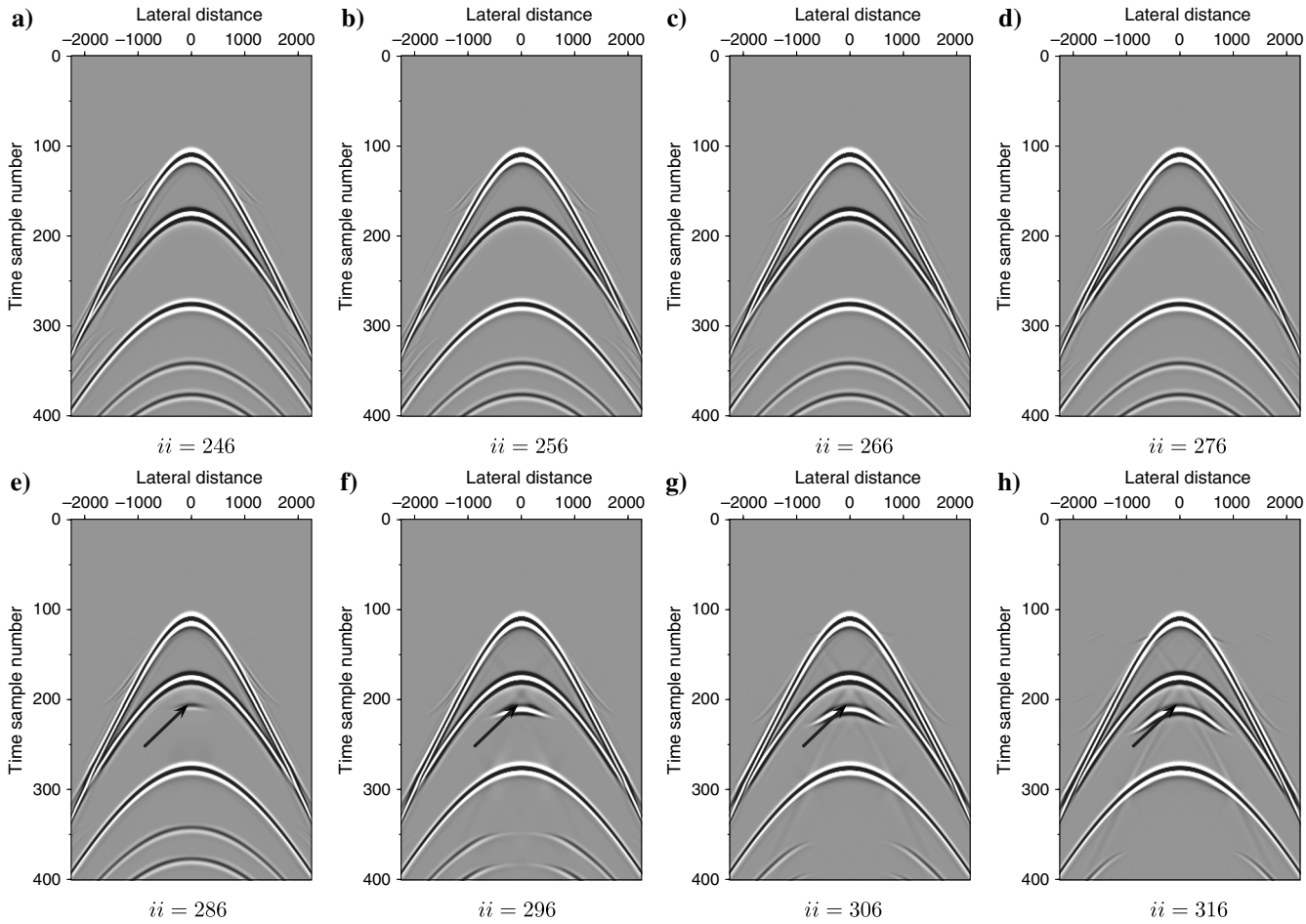

Figure 11. The term k_1^- after 32 iterations with different time instants $ii = 246$ to $ii = 316$ with steps of 10 samples. From each panel, a constant-time cross section is selected at ii and all of these cross sections make up the multiple-free data. The arrows point to an event that compensates all internal multiples created between the second and third reflectors.

Figure 12. Compensation of internal multiples by events (colored lines) that are created by the Marchenko method, applied for a point (a) above and (b) below the third reflector. The three reflectors are numbered from top to bottom.

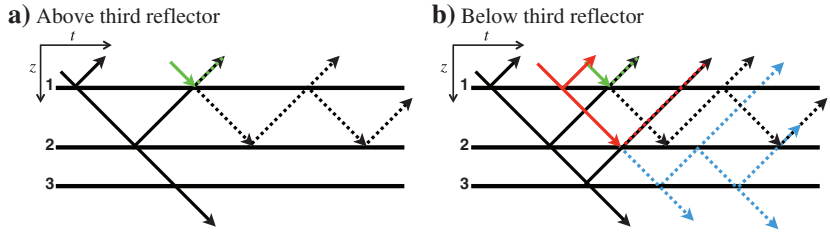

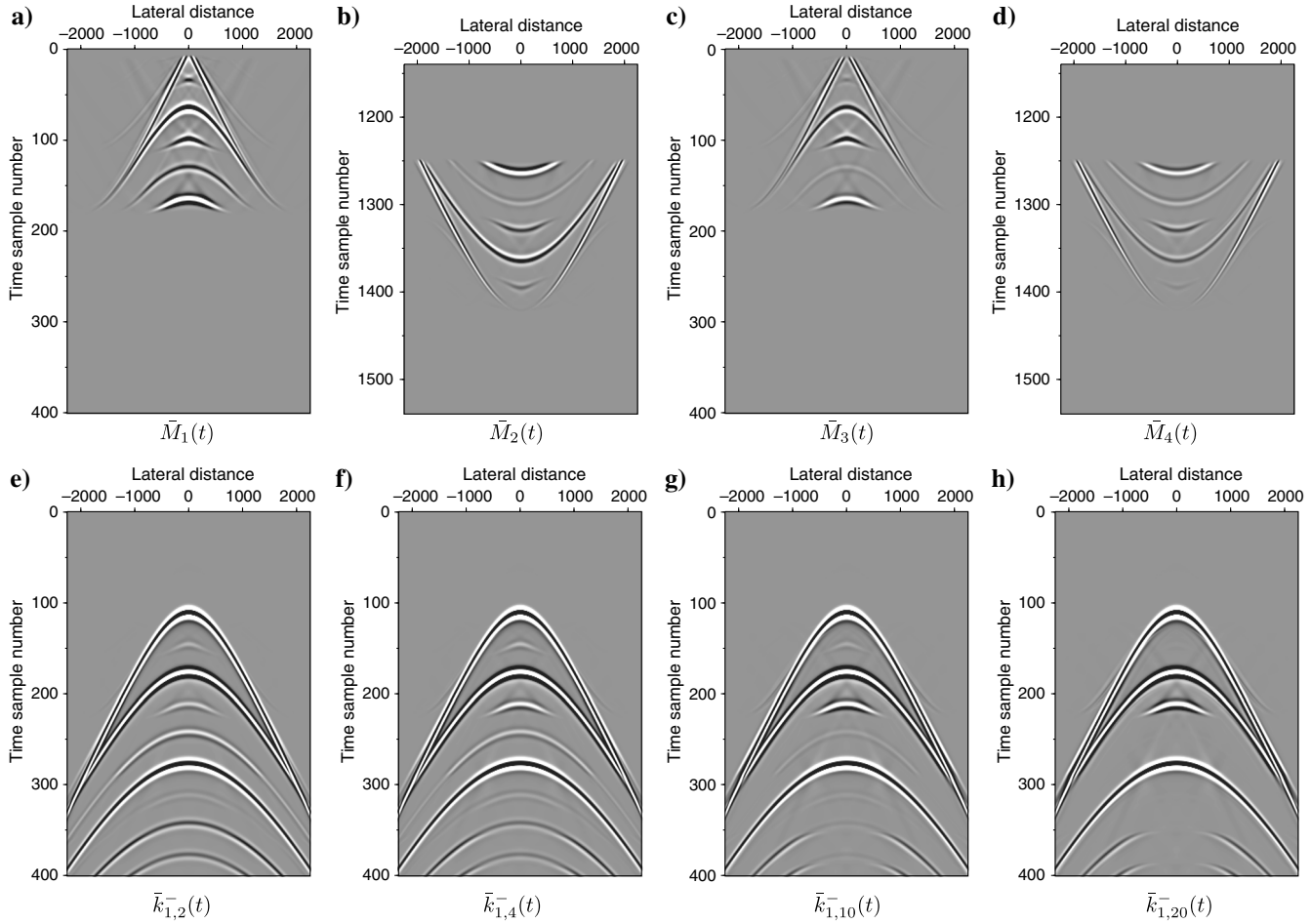

Figure 13. (a)–(d) The $\bar{M}_i$ fields for a focal time at sample $t_2 = 276$ with the transmission-compensated scheme T-MME after $i = 1, 2, 3, 4$ iterations. (e)–(h) The $\bar{k}^-_i$ fields for a focal time at sample $t_2 = 276$ with the transmission-compensated scheme T-MME after $i = 2, 4, 10, 20$ iterations. All figures are plotted with the same clipping factor.

flector. This event is also reflected by the second reflector (the upward red arrow) and creates the nonphysical reflection event observed in Figure 11e–11h and pointed out by an arrow.

Figure 13a–13d shows the same pictures as in Figure 9a–9d and Figure 13e–13h shows the same as Figure 10b, 10d, 10f, and 10h, but now with the T-MME scheme (Zhang et al., 2019). The T-MME scheme for time sample 276 includes the reflection of the third reflector because the time window is now $276 + n_\varepsilon$. This extra reflector introduces new events in $\bar{M}_i$. In the $\bar{k}^-_{1,i}$ terms, the nonphysical primary, just below the second reflector, is clearly visible. After 20 iterations, Figure 13h looks very similar to Figure 11f (time instant 296). The difference is that in the T-MME scheme the truncation starts at $t_2 + \varepsilon$ (sample 276+8) and the value at t_2 (time sample 276) is exactly right in v^- for the local reflection coefficient and stored in the final data output ($R_r[276]$), whereas, in the MME scheme of Figure 11g, the truncation starts at $t_2 - \varepsilon$ (sample 296–8) and the value at t_2 (time sample 296) in u^- is the correct value for the physical primary and is stored in the final data output ($R_t[296]$).

In the example for the MME scheme, we have shown (in equation 20) that the reflection strength of the second reflector was modified in v_1^- from its physical amplitude to its local reflection coefficient as the amplitude. It is exactly this feature that T-MME exploits. When the Marchenko schemes reach the arrival time of a reflector, there is a decision to be made where to put the reflection of that reflector. Setting the truncation time to $t_2 - \varepsilon$, the time instant t_2 is correctly obtained in u_1^-. Changing the truncation time from $t_2 - \varepsilon$ to $t_2 + \varepsilon$, the time instant t_2 is correctly obtained in v_1^- instead of in u_1^-. It is the time duration of the source wavelet that allows us to make this choice. By taking $t_2 - \varepsilon$, an error is introduced in v_1^- and hence u_1^- is correct at t_2, whereas by taking $t_2 + \varepsilon$ the error is in u_1^- and v_1^- will be correct at t_2.

The transmission-compensated (T-MME) scheme retrieves primary reflections with local reflection coefficients, whereas, in the regular (MME) scheme, the primary reflections keep their two-way reflection coefficients that include transmission losses. The local reflection retrieval of the T-MME scheme is exact for a horizontally layered medium, but, in laterally varying media, it is approximately true (Zhang et al., 2019). The only computational difference between the T-MME and MME schemes is the position of the time-truncation window.

CONCLUSION

In this paper, we have demonstrated step by step the correct and effective elimination of internal multiple reflections from the acoustic reflection response using the truncation time instant as a free

parameter. With a simple four-layer model, we showed that in a 1.5D model MME retrieves the primary reflections with their physical amplitude whereas T-MME retrieves the primary reflections with their local reflection coefficient. The examples also show that, when a first-order internal multiple is eliminated, the whole train of multiples associated with that first-order multiple is eliminated as well. This is achieved by a single multiple annihilator that is computed from only primary reflections in the data. The compute kernels of the two schemes are identical and consist of a matrix vector product that alternates between a time correlation and a time convolution. Exact and efficient computation of the discrete correlations and convolutions is done with an FFT routine. The only difference between MME and T-MME is the implementation of the time truncation. MME excludes a chosen time window before the truncation time instant and obtains the result after the scheme has converged by evaluating the equation at the truncation time instant. T-MME includes a chosen time window after that time instant and obtains the result directly from the value at the truncation time instant when the scheme has converged. For each truncation time instant, the iterative scheme computes the multiple annihilators and the corresponding reflection output. The current standard implementation takes every data time sample as a truncation time; the faster implementation can take larger time steps for the truncation time by exploiting the finite frequency bandwidth of the data.

ACKNOWLEDGMENTS

The research of J. Thorbecke and K. Wapenaar has received funding from the European Research Council (ERC) under the European Union's Horizon 2020 research and innovation program (grant no. 742703). We would like to thank the associate editor and the three anonymous reviewers for their constructive comments and efforts to compile the code and reproduce the figures.

DATA AND MATERIALS AVAILABILITY

Data associated with this research are available and can be accessed via the following URL: 10.5281/zenodo.4271598.

REFERENCES

Behura, J., K. Wapenaar, and R. Snieder, 2014, Autofocus imaging: Image reconstruction based on inverse scattering theory: Geophysics, **79**, no. 3, A19–A26, doi: 10.1190/geo2013-0398.1.

Brackenhoff, J., J. Thorbecke, and K. Wapenaar, 2019, Virtual sources and receivers in the real earth — Considerations for practical applications: Journal of Geophysical Research, Solid Earth, **124**, 11802–11821, doi: 10.1029/2019JB018485.

Broggini, F., R. Snieder, and K. Wapenaar, 2014, Data-driven wave field focusing and imaging with multidimensional deconvolution: Numerical examples from reflection data with internal multiples: Geophysics, **79**, no. 3, WA107–WA115, doi: 10.1190/geo2013-0307.1.

Cohen, J. K., and J. W. Stockwell, 2016, CWP/SU: Seismic Un*x Release No. 43R4: An open source software package for seismic research and processing: Center for Wave Phenomena, Colorado School of Mines.

da Costa Filho, C. A., G. A. Meles, A. Curtis, M. Ravasi, and A. Kritski, 2017, Imaging strategies using Marchenko focusing functions: 79th Annual International Conference and Exhibition, EAGE, Extended Abstracts, Tu P9 15, doi: 10.3997/2214-4609.201701131.

da Costa Filho, C. A., M. Ravasi, A. Curtis, and G. A. Meles, 2014, Elastodynamic Green's function retrieval through single-sided Marchenko inverse scattering: Physical Review E, **90**, 063201, doi: 10.1103/PhysRevE.90.063201.

Dukalski, M. S., and K. de Vos, 2017, Marchenko inversion in a strong scattering regime including surface-related multiples: Geophysical Journal International, **212**, 760–776, doi: 10.1093/gji/ggx434.

Jia, X., A. Guitton, and R. Snieder, 2018, A practical implementation of subsalt Marchenko imaging with a Gulf of Mexico data set: Geophysics, **83**, no. 5, S409–S419, doi: 10.1190/geo2017-0646.1.

Lomas, A., and A. Curtis, 2019, An introduction to Marchenko methods for imaging: Geophysics, **84**, no. 2, F35–F45, doi: 10.1190/geo2018-0068.1.

Lomas, A., S. Singh, and A. Curtis, 2020, Imaging vertical structures using Marchenko methods with vertical seismic-profile data: Geophysics, **85**, no. 2, S103–S113, doi: 10.1190/geo2018-0698.1.

Matias, M. A., R. Pestana, and J. van der Neut, 2018, Marchenko imaging by unidimensional deconvolution: Geophysical Prospecting, **66**, 1653–1666, doi: 10.1111/1365-2478.12686.

Meles, G. A., C. A. da Costa Filho, and A. Curtis, 2017, Synthesising singly-scattered waves (primaries) from multiply-scattered data: 79th Annual International Conference and Exhibition, EAGE, Extended Abstracts, Tu P4 11, doi: 10.3997/2214-4609.201701056.

Meles, G. A., K. Löer, M. Ravasi, A. Curtis, and C. A. da Costa Filho, 2015, Internal multiple prediction and removal using Marchenko autofocusing and seismic interferometry: Geophysics, **80**, no. 1, A7–A11, doi: 10.1190/geo2014-0408.1.

Meles, G. A., K. Wapenaar, and J. Thorbecke, 2018, Virtual plane-wave imaging via Marchenko redatuming: Geophysical Journal International, **214**, 508–519, doi: 10.1093/gji/ggy143.

Meles, G. A., L. Zhang, J. Thorbecke, K. Wapenaar, and E. Slob, 2020, Data-driven retrieval of primary plane-wave responses: Geophysical Prospecting, **68**, 1834–1846, doi: 10.1111/1365-2478.12960.

Mildner, C., F. Broggini, K de Vos, and J. O. A. Robertsson, 2019, Accurate source wavelet estimation using Marchenko focusing functions: Geophysics, **84**, no. 6, Q73–Q88, doi: 10.1190/geo2018-0726.1.

Pereira, R., M. Ramzy, P. Griscenco, B. Huard, H. Huang, L. Cypriano, and A. Khalil, 2019, Internal multiple attenuation for OBN data with overburden/target separation: 89th Annual International Meeting, SEG, Expanded Abstracts, 4520–4524, doi: 10.1190/segam2019-3215138.1.

Ravasi, M., 2017, Rayleigh-Marchenko redatuming for target-oriented, true-amplitude imaging: Geophysics, **82**, no. 6, S439–S452, doi: 10.1190/geo2017-0262.1.

Ravasi, M., and I. Vasconcelos, 2020, PyLops — A linear-operator Python library for scalable algebra and optimization: SoftwareX, **11**, 100361, doi: 10.1016/j.softx.2019.100361.

Ravasi, M., I. Vasconcelos, A. Kritski, A. Curtis, C. A. da Costa Filho, and G. A. Meles, 2016, Target-oriented Marchenko imaging of a North Sea field: Geophysical Journal International, **205**, 99–104, doi: 10.1093/gji/ggv528.

Singh, S., R. Snieder, J. Behura, J. van der Neut, K. Wapenaar, and E. Slob, 2015, Marchenko imaging: Imaging with primaries, internal multiples, and free-surface multiples: Geophysics, **80**, no. 5, S165–S174, doi: 10.1190/geo2014-0494.1.

Singh, S., R. Snieder, J. van der Neut, J. Thorbecke, E. Slob, and K. Wapenaar, 2017, Accounting for free-surface multiples in Marchenko imaging: Geophysics, **82**, no. 1, R19–R30, doi: 10.1190/geo2015-0646.1.

Slob, E., 2016, Green's function retrieval and Marchenko imaging in a dissipative acoustic medium: Physical Review Letters, **116**, 164301, doi: 10.1103/PhysRevLett.116.164301.

Slob, E., K. Wapenaar, F. Broggini, and R. Snieder, 2014, Seismic reflector imaging using internal multiples with Marchenko-type equations: Geophysics, **79**, no. 2, S63–S76, doi: 10.1190/geo2013-0095.1.

Sripanich, Y., I. Vasconcelos, and K. Wapenaar, 2019, Velocity-independent Marchenko focusing in time- and depth-imaging domains for media with mild lateral heterogeneity: Geophysics, **84**, no. 6, Q57–Q72, doi: 10.1190/geo2019-0059.1.

Staring, M., R. Pereira, H. Douma, J. van der Neut, and K. Wapenaar, 2018, Source-receiver Marchenko redatuming on field data using an adaptive double-focusing method: Geophysics, **83**, no. 6, S570–S590, doi: 10.1190/geo2017-0796.1.

Thorbecke, J., and J. Brackenhoff, 2020, OpenSource code for finite difference, Marchenko and utilities, https://github.com/JanThorbecke/OpenSource, doi: 10.5281/zenodo.4271598.

Thorbecke, J., and D. Draganov, 2011, Finite-difference modeling experiments for seismic interferometry: Geophysics, **76**, no. 6, H1–H18, doi: 10.1190/geo2010-0039.1.

Thorbecke, J., E. Slob, J. Brackenhoff, J. van der Neut, and K. Wapenaar, 2017, Implementation of the Marchenko method: Geophysics, **82**, no. 6, WB29–WB45, doi: 10.1190/geo2017-0108.1.

Van der Neut, J., I. Vasconcelos, and K. Wapenaar, 2015b, On Green's function retrieval by iterative substitution of the coupled Marchenko equations: Geophysical Journal International, **203**, 792–813, doi: 10.1093/gji/ggv330.

Van der Neut, J., and K. Wapenaar, 2016, Adaptive overburden elimination with the multidimensional Marchenko equation: Geophysics, **81**, no. 5, T265–T284, doi: 10.1190/geo2016-0024.1.

Verschuur, E., A. Berkhout, and K. Wapenaar, 1992, Adaptive surface-related multiple elimination: Geophysics, **57**, 1166–1177, doi: 10.1190/1.1443330.

Wapenaar, K., 2014, Single-sided Marchenko focusing of compressional and shear waves: Physical Review E, **90**, 063202, doi: 10.1103/PhysRevE.90.063202.
Wapenaar, K., J. Thorbecke, J. van der Neut, F. Broggini, E. Slob, and R. Snieder, 2014a, Green's function retrieval from reflection data, in absence of a receiver at the virtual source position: The Journal of the Acoustical Society of America, **135**, 2847–2861, doi: 10.1121/1.4869083.
Wapenaar, K., J. Thorbecke, J. van der Neut, F. Broggini, E. Slob, and R. Snieder, 2014b, Marchenko imaging: Geophysics, **79**, no. 3, WA39–WA57, doi: 10.1190/geo2013-0302.1.
Wapenaar, K., J. Thorbecke, J. van der Neut, E. Slob, and R. Snieder, 2017, Virtual sources and their responses — Part 2: Data-driven single-sided focusing: Geophysical Prospecting, **65**, 1430–1451, doi: 10.1111/1365-2478.12495.
Wapenaar, K., and J. van IJsseldijk, 2020, Discrete representations for Marchenko imaging of imperfectly sampled data: Geophysics, **85**, no. 2, A1–A5, doi: 10.1190/geo2019-0407.1.
Zhang, L., and E. Slob, 2019, Free-surface and internal multiple elimination in one step without adaptive subtraction: Geophysics, **84**, no. 1, A7–A11, doi: 10.1190/geo2018-0548.1.
Zhang, L., and E. Slob, 2020a, A field data example of Marchenko multiple elimination: Geophysics, **85**, no. 2, S65–S70, doi: 10.1190/geo2019-0327.1.
Zhang, L., and E. Slob, 2020b, A fast algorithm for multiple elimination and transmission compensation in primary reflections: Geophysical Journal International, **221**, 371–377, doi: 10.1093/gji/ggaa005.
Zhang, L., and E. Slob, 2020c, Marchenko multiple elimination of a laboratory example: Geophysical Journal International, **221**, 1138–1144, doi: 10.1093/gji/ggaa062.
Zhang, L., and M. Staring, 2018, Marchenko scheme based internal multiple reflection elimination in acoustic wavefield: Journal of Applied Geophysics, **159**, 429–433, doi: 10.1016/j.jappgeo.2018.09.024.
Zhang, L., J. Thorbecke, K. Wapenaar, and E. Slob, 2019, Transmission compensated primary reflection retrieval in data domain and consequences for imaging: Geophysics, **84**, no. 4, Q27–Q36, doi: 10.1190/geo2018-0340.1.

Jan Thorbecke received an M.S. (1991) and a Ph.D. (1997) in applied physics (geophysics) from the Delft University of Technology. From 1996 to 2001, he worked at Cray/SGI as a geophysical application engineer. From 2001 to 2002, he worked at Jason Geosystems, and since 2002, he has worked at HPE-Cray as an application analyst (0.8) and senior researcher at the Delft University of Technology (0.2). He has organized several conference workshops related to high-performance computing. In 2012, he has been awarded as GEOPHYSICS reviewer of the year. In 2020, he became distinguished technologist at HPE-Cray. His research interests include wavefield extrapolation, wavefield modeling, multidimensional convolution, and compute efficient algorithm design and implementation on supercomputers.

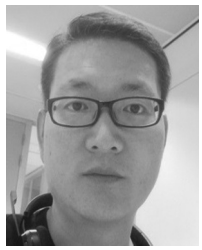

Lele Zhang received a doctorate degree (2019) in applied sciences from the Delft University of Technology (TU Delft), the Netherlands. Since the beginning of 2020, he has worked as a postdoctoral research fellow in the Department of Geosciences and Engineering at TU Delft. He has organized several international workshops and conference sessions and was guest editor for one special journal issue on multiple reflections in geophysics. His research interests include signal processing, wavefield propagation, and migration.

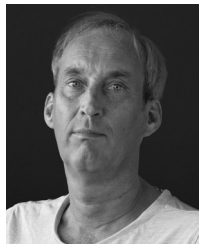

Evert Slob received a doctorate degree (1994, cum laude) in applied sciences from the Delft University of Technology (TU Delft), the Netherlands. From 1995 to 2011, he was research fellow, assistant, and associate professor, and since 2011, he has been a professor in the Department of Geosciences and Engineering at TU Delft. He was the general chair of the 10th International Conference on GPR in 2004. He served as a director of education of Civil Engineering and Geosciences from 2014 to 2018. He organized more than a dozen international workshops and conference sessions and was guest editor for 11 special journal issues on GPR and hydrogeophysics. He is a coauthor of *Introduction to controlled-source electromagnetic methods* published in 2019. He is a coeditor of *Seismoelectric exploration* published in 2020. He was the SEG Editor from 2013 to 2015, and he received the Reginald Fessenden Award from SEG in 2020.